



HAL
open science

Selective laser melting of WC reinforced maraging steel 300: Microstructure characterization and tribological performance

Xingchen Yan, Chaoyue Chen, Ruixin Zhao, Wenyou Ma, Rodolphe Bolot, Jiang Wang, Zhongming Ren, Hanlin Liao, Min Liu

► To cite this version:

Xingchen Yan, Chaoyue Chen, Ruixin Zhao, Wenyou Ma, Rodolphe Bolot, et al.. Selective laser melting of WC reinforced maraging steel 300: Microstructure characterization and tribological performance. *Surface and Coatings Technology*, 2019, 371, pp.355 - 365. 10.1016/j.surfcoat.2018.11.033 . hal-03486964

HAL Id: hal-03486964

<https://hal.science/hal-03486964>

Submitted on 20 Dec 2021

HAL is a multi-disciplinary open access archive for the deposit and dissemination of scientific research documents, whether they are published or not. The documents may come from teaching and research institutions in France or abroad, or from public or private research centers.

L'archive ouverte pluridisciplinaire **HAL**, est destinée au dépôt et à la diffusion de documents scientifiques de niveau recherche, publiés ou non, émanant des établissements d'enseignement et de recherche français ou étrangers, des laboratoires publics ou privés.



Distributed under a Creative Commons Attribution - NonCommercial 4.0 International License

Selective laser melting of WC reinforced maraging steel 300: microstructure characterization and tribological performance

Xingchen YAN^{a,b#}, Chaoyue CHEN^{a,c##}, Ruixin ZHAO^c, Wenyu MA^b, Rodolphe BOLOT^a, Jiang WANG^{c**}, Zhongming REN^c, Hanlin LIAO^a, Min LIU^b

a. *LERMPS, ICB UMR 6303, CNRS, Univ. Bourgogne Franche-Comté, UTBM, F-90010 Belfort, France*

b. *National Engineering Laboratory for Modern Materials Surface Engineering Technology; The Key Lab of Guangdong for Modern Surface Engineering Technology; Guangdong Institute of New Materials, Guangzhou 510651, P.R. China*

c. *State Key Laboratory of Advanced Special Steels, School of Materials Science and Engineering, Shanghai University, Shanghai 200444, China*

Abstract: Owing to the limited wear resistance, Maraging steels has limited applications in the harsh environments, leading to a shortened service-life or even failure. In this study, WC particles reinforced maraging steel 300 (MS300) composites were produced by selective laser melting (SLM) to enhance the tribological performance. The microstructure and phase analysis of SLM-produced composites were investigated by SEM-EDS. Dry sliding wear test and microhardness were used to investigate the mechanical properties of WC/MS300 composites. As laser energy density increases, the microhardness drops rapidly and the maximum value of 562.2 HV₂ was measured at the linear energy density of 110 J/m. Dry sliding tests show that the wear rate was decreased by more than 1500 times through the WC reinforcement compared with pure MS300 sample, which emphasizes the superior wear-resistance properties of MS300/WC composite. Besides, the best wear-resistance performance at the improved linear energy density of 125 J/m. The study on wear mechanism shows that formation of carbide layer between WC and MS300 matrix significantly prevent the plowing effect. The present work provides an effectively method to improve the tribological performance MS300 through the reinforcement of WC particle by selective laser melting.

Keywords: Selective laser melting (SLM); WC; Maraging steel 300; tribological behavior

1 **1. Introduction**

2 The selective laser melting (SLM) as an additive manufacturing technology, has been widely applied
3 in different areas [1-3]. SLM technique allows the manufacturing of net-shape components directly from
4 powder material according to the computer-aided design (CAD) model. In this process, the designed model
5 is firstly sliced into a series of layers with constant thickness. Then, the part is fabricated by selectively
6 melting the powder bed by a traverse laser source, and the formed molten pool will experience rapid-
7 solidification at a high cooling rate. This technology enables the fabrication of customized or personalized
8 part within a wide range of areas like biomedical [4], aeronautics and astronautics [5, 6].

9 Based on the principle of precipitation hardening, the Maraging steel 300 (MS300) exhibits
10 outstanding material properties like high strength, high ductility and superior machinability [7-9]. It has
11 been widely used as engine component, missile parts, aircrafts, oil and gas industries [10, 11]. The
12 application of SLM technique in the fabrication of molding can significantly shorten the preparation period
13 and the production cycle, which enables the rapid innovation and production of molding design.
14 Furthermore, the SLM technique can achieve the production of customized molding with complex
15 geometry. For example, Kempen and Hermann [8, 12] have investigated the mechanical properties and
16 microstructures of Maraging steel 300 (MS300) samples fabricated by SLM, which present high
17 densification rate and mechanical properties. Bai et al. [13] reported the effects of processing parameters
18 and heat treatment on the microstructure and mechanical properties of maraging steel 300 fabricated by
19 SLM. It is reported that the high-frequency friction of molding with counterpart can lead to its shortening
20 of service-life even the failing [14]. The limited wear resistance of Maraging steels has largely restricted its
21 applications in the harsh environments with wear and corrosion. Therefore, it is reasonable to improve the
22 wear behavior by adding the reinforcement particles to the Maraging materials to improve its wear-
23 resistance performance.

24 Based on the previous literatures, SLM technology has been used to fabricate metal matrix composites
25 (MMCs) with high performance [15-17]. The rapid melting and solidification can result in high mechanical
26 properties and homogenous microstructure of the reinforcement particles such as WC [18, 19], TiB₂ [20-
27 22], WC-CO, Al₂O₃ [23, 24], TiC [25]. For example, Rong et al [18] fabricated the WC/Inconel 718

1 composite by SLM at different process parameters. It shows that at the high microhardness of 393.2 HV
2 and a lowest coefficient of friction (COF) was obtained at the optimal scan speed of 450 mm/s. Besides,
3 based on AlSi10Mg and nano-scaled TiC ceramic particles, Gu et al [26] fabricated the Al nanocomposites
4 with a novel ring-structured TiC reinforcement. Compared to the unreinforced AlSi10Mg part, the TiC
5 reinforced nanocomposite exhibited elevated microhardness (188.3 HV) and tensile strength with a
6 reduction in elongation. Similarly, Gu et al [25] used nano-TiC reinforcements to improve the
7 microhardness and wear resistance of Ti matrix by SLM. Song et al [27] fabricated Fe-based
8 nanocomposites with micro Fe and nano-SiC particles by SLM, where uniform distribution of SiC particles
9 and homogeneous martensites were observed. Recently, Li et al [20] used nano-TiB₂ decorated AlSi10Mg
10 composite powders to fabricate a dense Al composite samples by SLM, which shows high fracture strength
11 and ductility.

12 Therefore, in the present work, the MS300 matrix reinforced by micro-sized WC particles were
13 produced by SLM at different linear energy density. The microstructure and phase analysis of the SLM
14 composites were made to understand the role of WC particles during the enhancement of mechanical
15 properties. Meanwhile, the microhardness and wear performance of the produced WC/MS300 composites
16 were investigated to understand the evolution of mechanical properties. Furthermore, the effect of linear
17 energy density on the wear performance of the WC/MS300 composites were studied and discussed.

18 **2. Experimental details**

19 The gas atomized maraging steel 300 powders (EOS GmbH, Germany) with spherical shapes and a
20 size distribution between 33 μm and 40 μm and the irregular WC powders (Jinlu Xiamen China) with a size
21 range of 1-6 μm were used as starting materials. The powder mixture with 85% of MS300 and 15% of WC
22 in weight percentage were mechanically mixed in a tumbling container for 200 mins prior to SLM
23 fabrication. The morphologies of different powders are shown in Fig. 1. The chemical composition of
24 MS300 powder is given in Table. 1. The cross-sectional morphology after etching is shown in Fig. 2 (a),
25 showing homogeneously distributed grains.

26 Table 1. Chemical composition of MS300 powder.

Element	Fe	Ni	Co	Mo	Ti	Al	Cr	C	Mn	Si
wt%	Rest	17-19	8.5-9.5	4.5-5.2	0.6-0.8	0.05-0.15	≤0.5	≤0.03	≤0.1	≤0.01

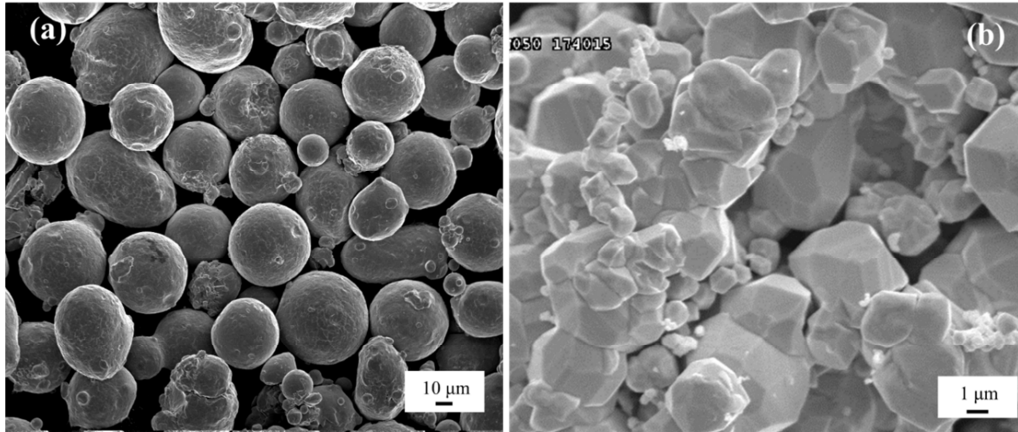
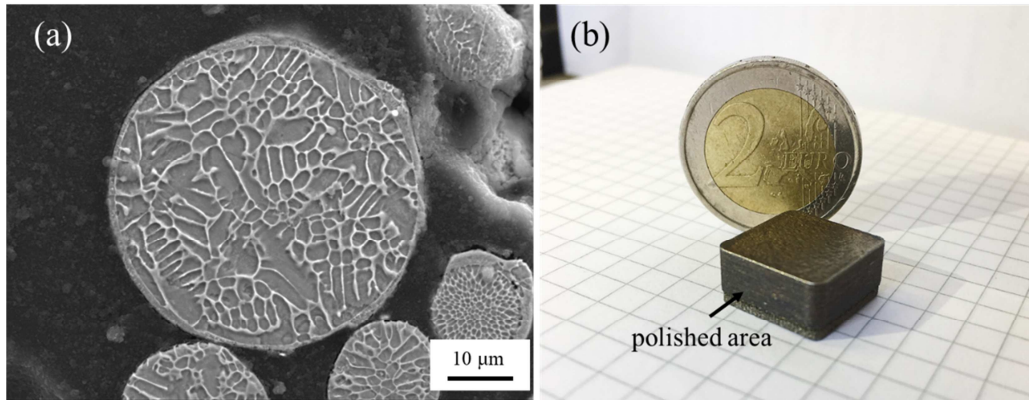


Fig. 1 SEM image of the powder morphologies: (a) MS300, (b) WC.

The sample annotations produced by SLM and the respective operating parameters are given in Table 2. In this work, the WC/MS300 composite were fabricated at different laser powers (190 - 280 W), whereas the pure MS300 sample were fabricated as a comparison object at the laser power of 220 W. It enabled us to investigate the role of WC reinforcement particle in the mechanical properties. A SLM machine (MCP-realizer SLM 250, Germany) was used to fabricate the WC/MS300 composite in this work, which was equipped with an YLR-100-SM single-mode CW ytterbium 400 W fiber laser. The laser beam diameter was set to 40 µm. The SLM process is realized within working chamber (250 mm × 250 mm × 280 mm) with an argon atmosphere. The oxygen content was maintained below 0.2% to prevent the oxidation during fabrication. The cubic specimen (10 mm × 10 mm × 5 mm) as shown in Fig. 2 (b) were prepared by SLM. For the observation of microstructure evolution, the cross-sectional sample were polished and then etched in a solution of 25 ml HNO₃, 50 ml HCl and 1 g CuCl₂ in distilled water for 20 s. In addition, the microstructure was then observed by a scanning electron microscope (SEM) equipped with an energy-dispersive spectroscopy (EDS) unit (JSM5800LV, JEOL, Japan). Phase composition of the SLM-fabricated samples was performed by X-ray diffraction (XRD, Siemens, Germany) using a cobalt anticathode (k=1.78897 Å) operated at 35 kV and 40 mA.



1
2 Fig. 2 (a) Cross-section showing the grain structure of the feedstock of MS300 particle after etching, (b)
3 digital photo of the cubic sample.

4 The porosity level and densification rate were measured and calculated through image analysis (NIH
5 Image J, Software, USA), where the results were the average of 15 analyses. The Vickers hardness was
6 measured using a micro-hardness tester (Leiz-Wetzlar, Germany) at the cross-sections of the composite
7 samples at a load of 2 N and an indentation time of 25 s, and the final value is the mean of 15
8 measurements.

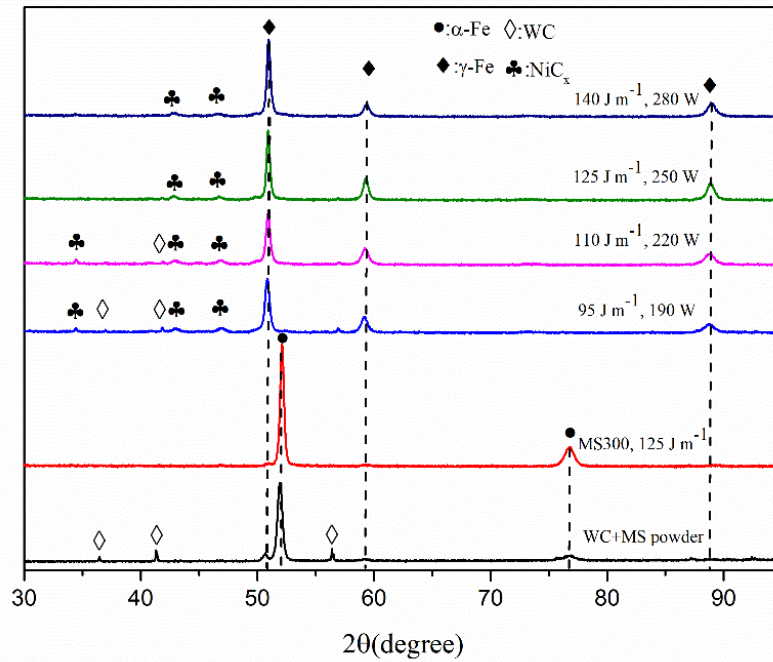
9 Table 2 Processing parameters and the designation of the fabricated samples in this work.

Number	Sample	Power (W)	Speed (m/s)	Linear energy density (J/m)
1	WC/MS300	190	2	95
2	WC/MS300	220	2	110
3	WC/MS300	250	2	125
4	MS300	250	2	125
5	WC/MS300	280	2	140

10 A tribometer implement (CSEM, Switzerland) was used to conduct the dry sliding wear tests at
11 ambient temperature. The surface roughness R_a below $0.15 \mu\text{m}$ was ensured to before the test. The cleaned
12 WC-Co balls with a diameter of 6 mm was used as the counterparts. The used processing parameters for the
13 friction test are given as below: load of 0.5 kg, rotational velocity of 0.1 m/s, sliding distance of 100 m, and
14 a friction radius of 3 mm. After the test, the variation of the coefficient of friction (COF) and the worn
15 morphology observed by SEM and EDS were analyzed to understand the wear performance. To calculate
16 the worn volume, the cross-sectional areas of the worn tracks were measured by an Altisurf 500
17 profilometer (France), the final value is the mean of 5 measurements.

1 3. Results and discussion

2 3.1. Phase analysis



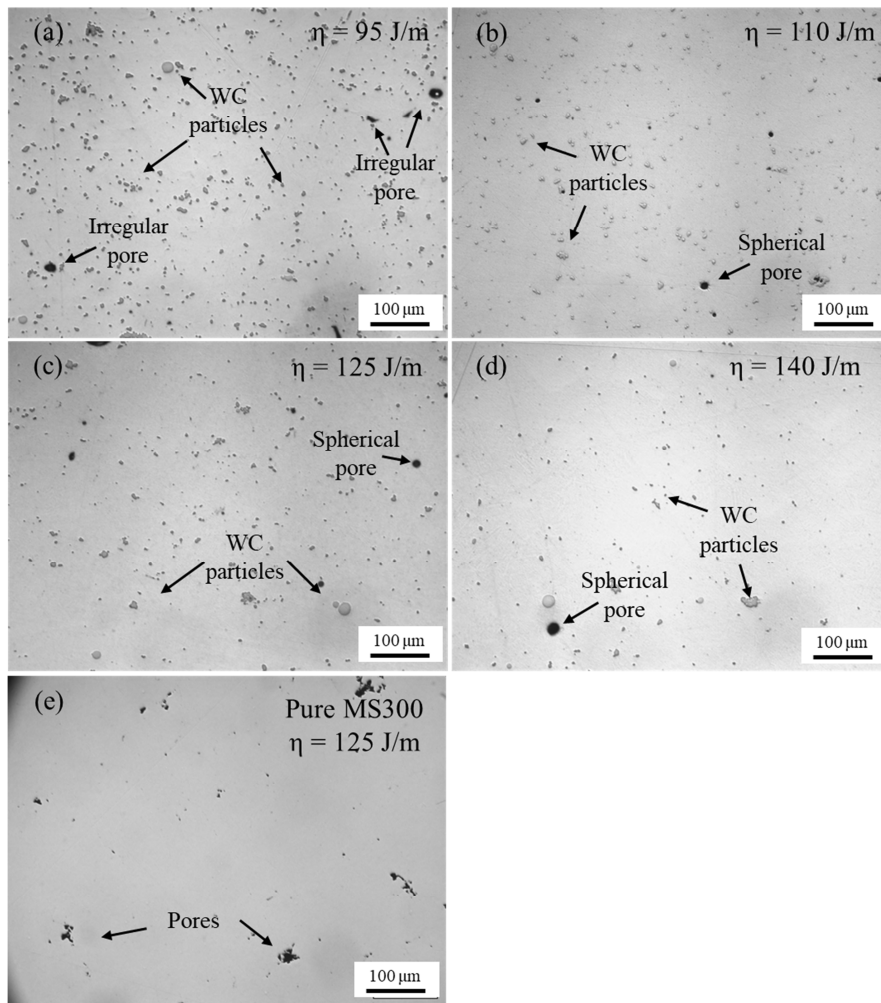
3

4 Fig. 3 XRD analysis of the feedstock powder, MS300/WC composite and pure MS300 samples processed
5 by SLM at different laser powers.

6 Fig. 3 gives the XRD spectra of SLM-processed WC/MS300 composites obtained within a wide range
7 between 30° and 95°. The main diffraction peaks corresponding to α -Fe (bcc) phase were detected in the
8 raw material and MS300 sample [8]. The peaks for WC can also be noticed in the raw powder. Significant
9 difference of XRD spectra can be found in the MS300/WC composite, where the α -Fe in MS300 was
10 transformed to the phase of γ -Fe (fcc). Chemical composition and formation temperature could influence
11 the transformation from high temperature γ -Fe to low temperature α -Fe [28]. In this study, the existence of
12 carbon content could hinder such transformation from γ -Fe to α -Fe. Besides, sub-cooling degree can greatly
13 affect the transformation of γ -Fe to the highly stained α -Fe. As the addition of WC particles with higher
14 conductivity, cooling rate of the molten pool for the composite part was improved compared with the pure
15 MS300. Consequently, γ -Fe was detected on the SLM MS300/WC parts instead of α -Fe in pure MS300 [29,
16 30]. Furthermore, the XRD characterization within small 2θ (35°-45°) angle should be noticed to

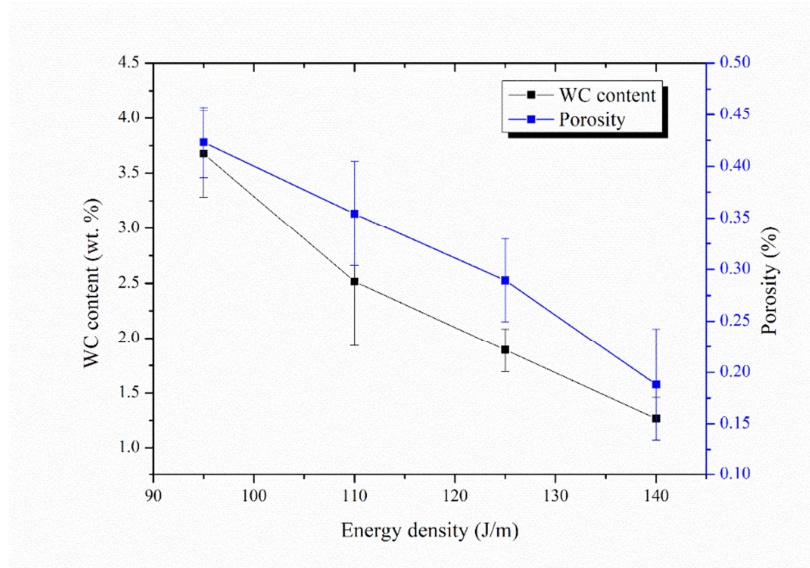
1 understand the influence of linear energy density on the WC particles. The WC phase is gradually
2 decreased as the increment of laser power. As for the linear energy density higher than 125 J/m, the WC
3 phase cannot be detected any more, which implied the decrement of WC particles. Due to the increasing
4 laser power, the WC particles were partially dissolved in the matrix. The residual amount of WC phase falls
5 out of the measurement range of XRD, which results in the vanishing of WC phase in XRD spectrum.

6 3.2. Microstructural analysis



7

8 Fig. 4 OM images of cross-sectional microstructure of the SLM-processed: MS300/WC samples at (a) 95
9 J/m, (b) 110 J/m, (c) 125 J/m, (d) 140 J/m, (e) pure MS300 sample at 125 J/m.

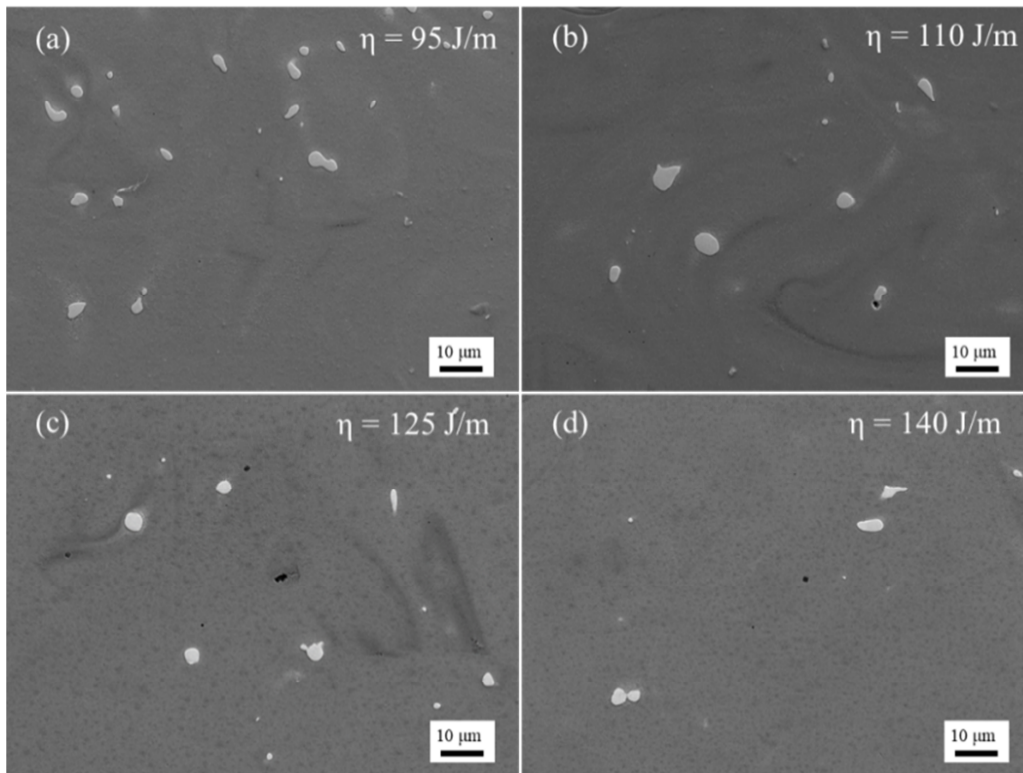


1

2

Fig. 5 Evolutions of porosity and the WC content of the WC/MS300 composite fabricated by SLM as a function of linear energy density.

3



4

5

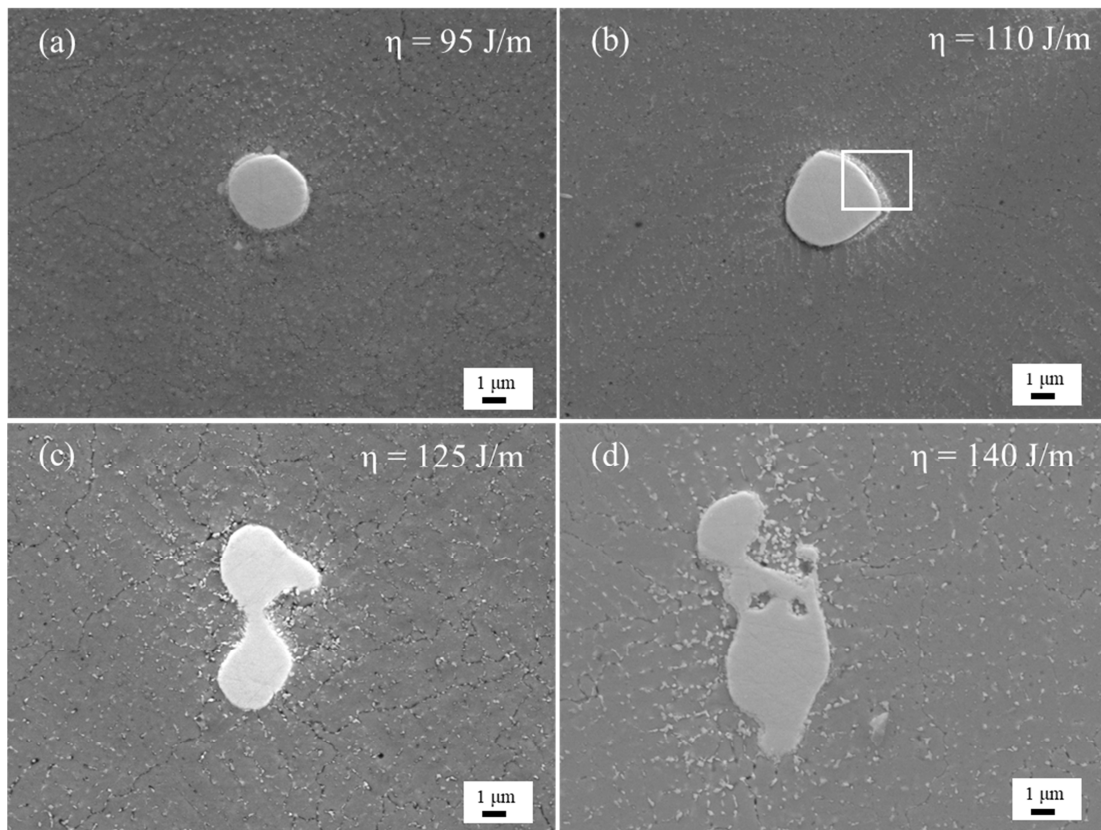
Fig. 6 Distribution of reinforcing particles of WC/MS300 composite fabricated at different laser power densities: (a) 95 J/m, (b) 110 J/m, (c) 125 J/m, (d) 140 J/m.

6

1 Fig. 4 shows the microstructure of the SLM processed MS300/WC composites at different energy
2 densities. The uniform distribution of WC particle can be seen in the OM images of MS300/WC samples. It
3 can be noticed that the WC particles are decreasing as a function of the linear energy density, which can be
4 attributed to the enhanced WC dissolution at higher molten pool temperature. Meanwhile, some irregular
5 pores can be seen on the cross-sectional images of the MS300/WC composite and the pure MS300 samples.
6 Based on Fig. 5, it can be observed that the porosity of the composite sample decreases as the laser power
7 increases. Furthermore, the morphology of pores changes from an irregular (Fig. 4 (a)) to a spherical shape
8 (Fig. 4 (b, c and d)). Moreover, the porosity of the pure MS300 sample fabricated at 125 J/m was
9 $0.83\pm 0.32\%$. As the magnified view is shown in Fig. 6, dense WC/MS300 composites were fabricated at
10 different energy densities with uniform distribution of reinforced particles. It can be noticed that the content
11 of WC particle in the MS300 matrix is decreasing as a function of increasing linear energy density. The
12 MS300 matrix experienced a complete melting under the high-energy input by laser beam, while the WC
13 particles experienced partial dissolution due to their relatively higher melting point. Similar result is also
14 obtained by XRD analysis (Fig. 3), the content ratio of WC particle in the composite was decreasing with
15 the increasing linear energy density. The weight ratio of WC particles in MS300 matrix is evaluated and
16 transformed from the analysis by the ImageJ software and given in Fig. 5. At the linear energy density of
17 95 J/m, the measured volume content of WC particles is 1.94 % and is far below the volume ratio of 9% in
18 starting materials, which indicates its partial dissolution into matrix. At the higher laser energy density η ,
19 less reinforced WC particles can be found in the MS300 matrix due to the enhanced particle dissolution at
20 higher temperature. At the same time, the higher temperature within the molten pool at a higher linear
21 energy density will lead to a stronger Marangoni flow, which is caused by the surface tension gradient
22 proportional to the temperature gradient. The role of Marangoni flow in the SLM process has been widely
23 studied in the numerical model [31, 32]. The increased temperature will reduce the viscosity of molten pool
24 [33], which can promote the flow fluid within the molten pool. Thus, the combined effects of increased
25 Marangoni flow and decreased molten pool viscosity can efficient improve the movement of the reinforced
26 WC particles within the molten pool as well as its solution into the matrix. It can directly lead to the
27 observed WC particles distribution in Fig. 6.

1 **3.3. WC particle evolution**

2 Fig. 7 presents the etched cross-section of the WC particles and the MS300 matrix at different laser
3 energy densities. Generally, it can be noticed that all the WC particles were well inserted in the MS300
4 matrix. At a relatively low η of 95 J/m, almost no diffusion layer can be seen surrounding the particles (Fig.
5 7 (a)). As the linear energy density η increased from 95 to 110 J/m, an evident gradient layer can be found
6 around the WC particles in the MS300 matrix, which consists of carbide phase with high hardness. By
7 further increasing the linear energy density to 125 J/m and 140 J/m, the fusion between two adjacent WC
8 particles can be observed due to the gradually increasing temperature and fluid flow within molten pool. At
9 the same time, the diffusion layer is not visible around the WC particles, while the diffusion region of
10 reinforced particles into the matrix material is more evident.



11

12 Fig. 7 Morphology of the reinforced WC particle and the diffusion layer around the particle at different
13 energy densities: (a) 95 J/m, (b) 110 J/m, (c) 125 J/m, (d) 140 J/m.

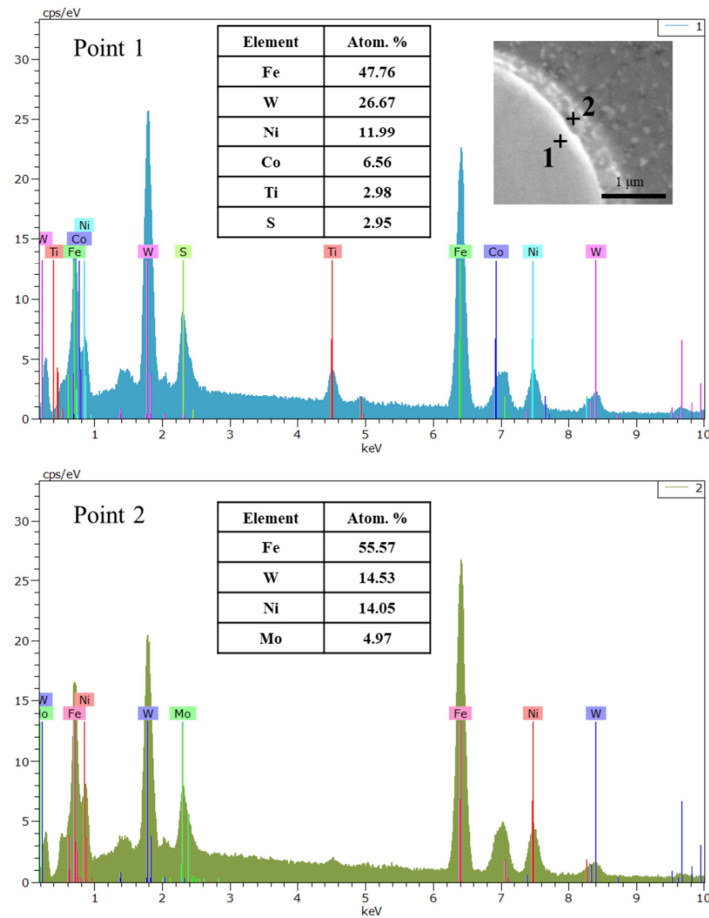


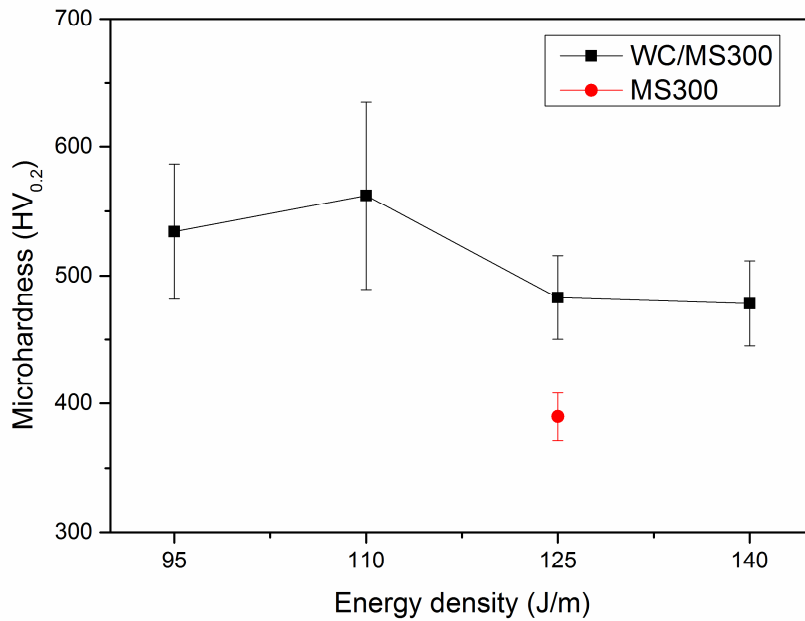
Fig. 8 Atomic percentages of the elements at points 1 and 2 in Fig. 8 (b) by EDS.

To investigate the chemical composition at the diffusion interlayer, the EDS analysis was carried out at the points 1 and 2 marked in magnified view in Fig. 7 (b). Fig. 8 presents the corresponding EDS results, showing the chemical composition at the diffusion region. It can be noticed that the magnified dissolution region can be seen at the periphery of WC particle imbedding in the MS300 matrix in Fig. 8 (a). Furthermore, continuous shell and disconnected globular dendrite are seen surrounding WC particle. Based on our previous study [34], the W elements were uniformly diffused from the reinforcement particle into matrix through this interlayer. Thus, based on the related studies, it is reasonable to suggest that the carbides (Fe_3W_3C , Fe_4W_2C or Fe_6W_6C [35]) were formed through the in-situ reaction between the WC particle and the element from matrix. The release and solution of W and C into the molten pool during SLM process can promote the solid solution hardening through the dislocation by precipitates [36]. Furthermore, the partial dissolution of WC particle with good wettability can effectively increase its contact

1 interface in the matrix molten pool, which can further improve the mechanical strength of composite. In
2 addition, it can be found that at the point 1 of the gradient interface, the atomic percentages of Fe and Ni
3 are 47.76 and 11.99 respectively, as the one of W is 26.67. The samples were covered by a thin conductive
4 layer by carbon sputtering prior to the SEM observation, so that the detection of C element in EDS is not
5 available in this work. Meanwhile, similar element types were found at the point 2 of diffusion layer with
6 large difference in the atomic percentage from the point 1. In the diffusion layer, the W element possessed
7 an atomic percentage of 14.57, which showed a decreased concentration compared to the gradient interface.
8 Meanwhile, the EDX results show that the content of Fe element gradually increases from the WC particle
9 to the matrix. Such features demonstrate a typical gradient interface between particle and matrix. Besides, it
10 should be noticed that the WC particle has experienced a partial dissolution, resulting a distinct shape
11 change. Different from the original sharp-shaped features, the WC particles embedded in matrix
12 demonstrate rounded shapes caused by the partial dissolution.

13 **3.4. Microhardness**

14 Fig. 9 shows the microhardness values of the WC/MS300 composite sample fabricated at different
15 linear laser energy density of η . By increasing the applied η from 95 J/m to 110 J/m, the average
16 microhardness value was slightly enhanced from 534.1 ± 52.4 HV2 to 562.2 ± 62.8 HV2. Such microhardness
17 enhancement was attributed to the more evident densification effect at higher linear energy density. By
18 further improving the implemented η to 125 J/m, an apparent microhardness drop can be seen. At the
19 applied η of 140 J/m, the microhardness continues to decrease to 478.2 ± 33.2 HV2. Such decrement of
20 microhardness at high linear energy density is considered as the combination effects of the decline of the
21 metastable stiff phase and the coarsened microstructure. As indicated in the XRD analysis in Fig. 3, the
22 metastable stiff phase of NiC_x is decreasing as the increment of linear energy density. Meanwhile, as shown
23 in Fig. 7, at the relatively high linear energy density, the overheating of the molten pool leads to the
24 formation of over coarsened microstructure. Thus, it is indicated that the microhardness of the composites
25 is directly influenced by the phase, grain size and defects in the matrix [18, 27]. By comparing the
26 WC/MS300 composites with the pure MS300 sample fabricated at the linear energy density of 125 J/m, it
27 can be found that the reinforcement of WC particles can significantly increase the microhardness through
28 the formation of the metastable stiff phase (NiC_x).



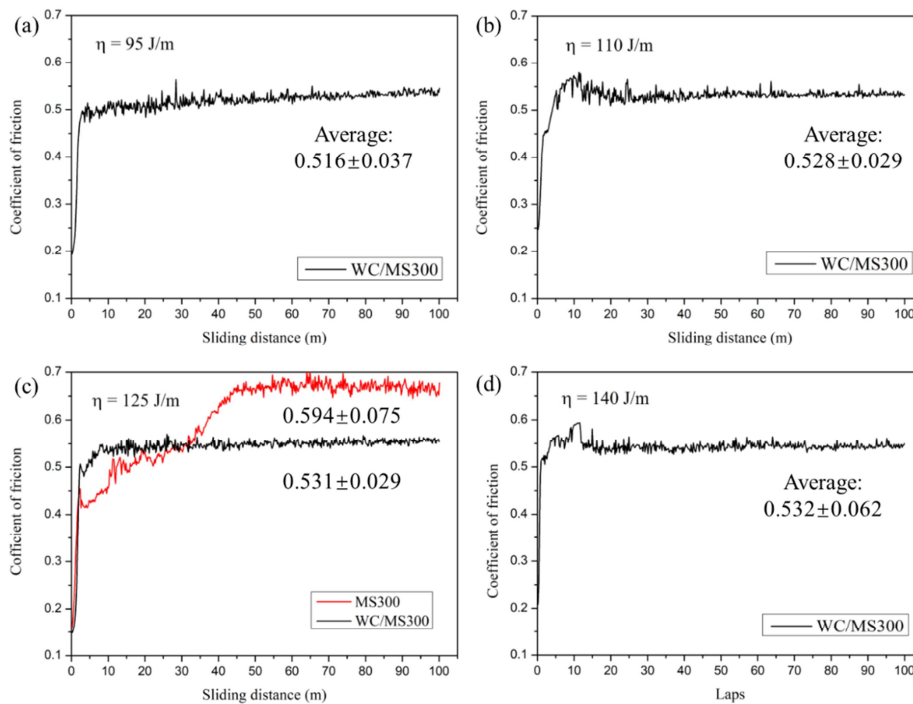
1
 2 Fig. 9 Microhardness of the WC/MS300 composites prepared at different energy densities and pure MS300
 3 sample at 125 J/m.

4 **3.5. Wear rate and morphology**

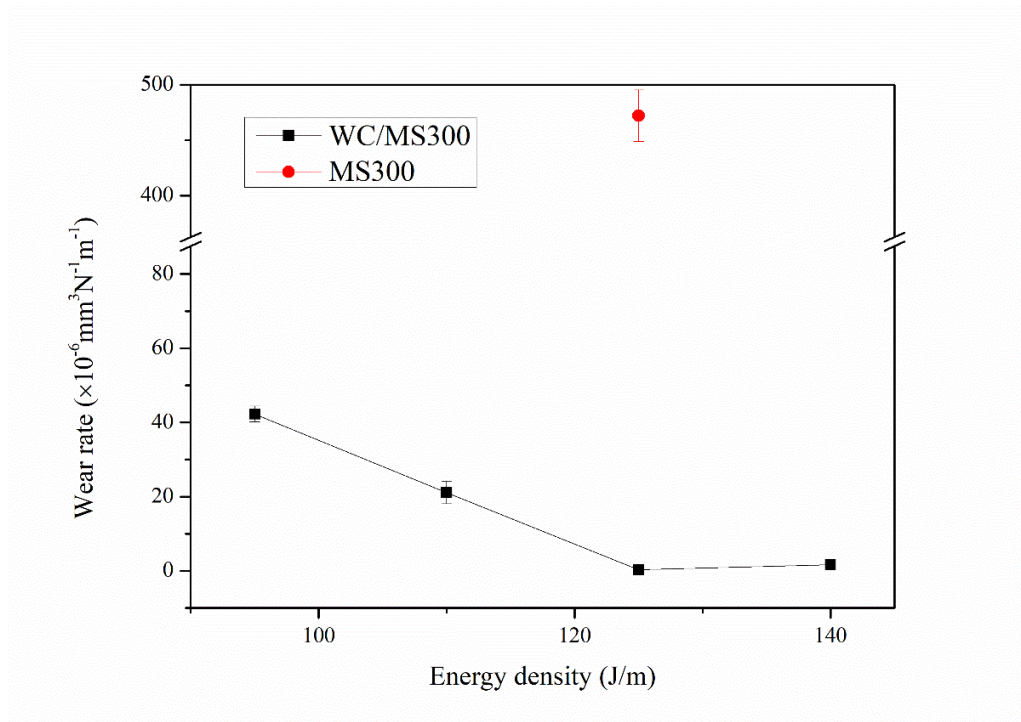
5 **3.5.1. Wear rate and coefficient of friction (COF)**

6 Fig. 10 and Fig. 11 show the evolution of COF with sliding distance and attendant wear rates for the
 7 WC/MS300 composites at different energy densities and for pure MS300 sample at 125 J/m. By comparing
 8 the WC/MS300 composites produced at different energy densities, the applied laser linear energy η played
 9 a key role in influencing the wear behavior of these composites. As can be seen from the COF curves, all
 10 WC/MS300 samples demonstrated stable variations with few fluctuations at the beginning stage. At a lower
 11 η of 95 J/m, the average COF value was 0.516 ± 0.037 , while the attendant wear rate reached as much as
 12 $42.27 \times 10^{-6} \text{ mm}^3/(\text{N} \cdot \text{m})$. However, a severe fluctuation of COF value was observed in Fig. 10. By
 13 increasing the η from 110 J/m to 125 J/m, the COF value increases from 0.54 to 0.53 and the resultant wear
 14 rate was reduced from $21.08 \times 10^{-6} \text{ mm}^3/(\text{N} \cdot \text{m})$ to $0.29 \times 10^{-6} \text{ mm}^3/(\text{N} \cdot \text{m})$, where fewer COF fluctuation can
 15 be found.

1 On the other hand, the pure MS300 sample is found to possess an evidently higher COF value and
 2 wear rate value ($472 \times 10^{-6} \text{ mm}^3/(\text{N} \cdot \text{m})$) than that of WC/MS300 composite ($0.29 \times 10^{-6} \text{ mm}^3/(\text{N} \cdot \text{m})$)
 3 fabricated at the same linear energy density. Such significant wear rate decrease (more than 2500 times)
 4 can further emphasize the role of reinforcement WC particles in the MS300 matrix in the wear performance.
 5 However, while the laser linear energy density η was further increased to 140 J/m, the COF value increased
 6 to 0.54 and wear rate increased to $1.65 \times 10^{-6} \text{ mm}^3/(\text{N} \cdot \text{m})$. It is obvious that the wear performance of the
 7 SLM-fabricated WC/MS300 composite is strongly affected by the applied linear energy density. The
 8 aggregated reinforcing particles also had significant influence on the unsteady COF values during the initial
 9 stage of friction test. At a relatively low energy input, the low wear behavior is mainly limited by the
 10 increase porosity level and bigger-sized WC. At a higher linear energy density, the densified microstructure
 11 and uniformly distributed reinforcement particles can result in a steady and lower COF value and lower
 12 wear rate.



13
 14 Fig. 10 COF value evolution of the samples prepared at different linear energy densities: (a) WC/MS300,
 15 95 J/m, (b) WC/MS300, 110 J/m, (c) WC/MS300 and MS300, 125 J/m, (d) WC/MS300, 140 J/m.



1

2

Fig. 11 Wear rate of the WC/MS300 composites and pure MS300 sample prepared at different linear

3

energy densities.

4

3.5.2. Wear trace

5

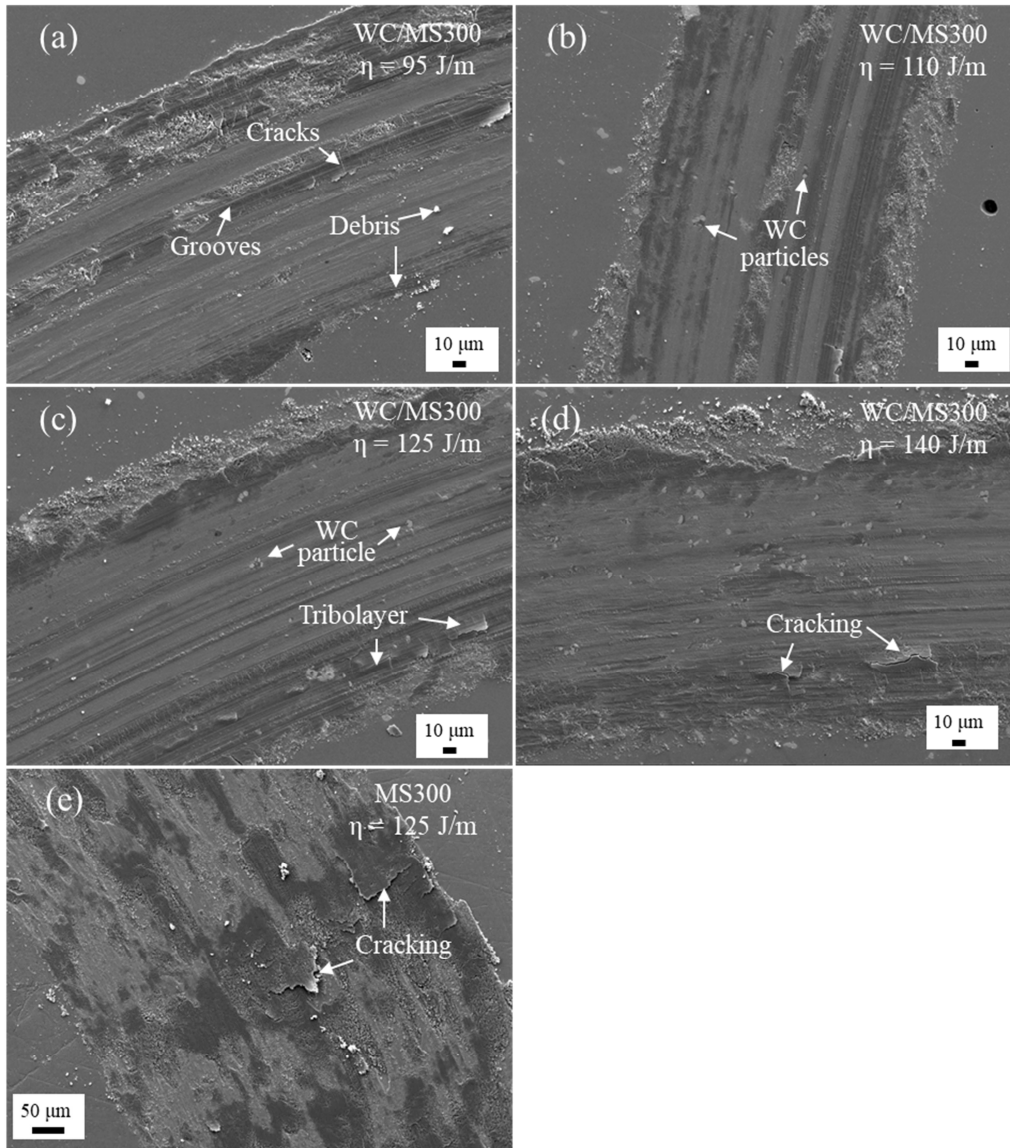
To provide a profound insight into the wear mechanism of WC/MS300 composite, the worn morphology was observed. Fig. 12 shows the characteristic morphologies of worn surfaces at different linear energy densities η . As shown in Fig. 12(a), parallel grooves were found on the worn surface fabricated at 95 J/m, which is the sign of abrasion wear. The rough and porous worn surface was scattered by shattered WC debris. Furthermore, accompanying gathering pores, the interface region between the WC and the matrix experienced evident cracking during the sliding process. By increasing η to 110 J/m, shallower grooves were found on the surface of worn tracks, as well as the existence of WC reinforcement particles with relatively complete shape. Such phenomena indicate that the bonding strength of the interface between WC and the matrix was reasonably enhanced owing to the higher linear energy density. However, the carbide stiff interface with uneven distribution was easily smashed when suffering the shear stress at the plowing surface, which is given in the magnified view (Fig. 13 (b)).

15

1 By increasing the η to 125 J/m, a smoothing and densified tribolayer was formed (Fig. 12 (c)). No sign
2 of plowing nor prominent WC particles can be seen on the worn surfaces. Such phenomena indicate the
3 change of wear mechanism from form abrasion to adhesion at a higher linear energy density. Meanwhile,
4 more W and C atoms from WC particle surface were released into the molten pool as can be seen from the
5 Fig. 7. It promotes their reaction with the major elements in MS300 like Fe and Ni, which leads to the
6 formation of the thick and even carbide layer around the WC particles. As the main composition of the
7 interfacial layer, the carbide layer observed in Fig. 7 can lead to the desired bonding between the WC
8 particles and the matrix. As a general understanding, the wear performance strongly depends on the bonding
9 strength between the reinforcements and the matrix. Therefore, the plowing effect of the WC particles on
10 the sliding surface that possess excellent bonding with the matrix was significantly decreased. Besides, as
11 shown in Fig. 13 (c), the WC particles and the in-situ formed interfacial layer did not experience splitting or
12 cracking during the test. On the contrary, the WC particles and the interfacial layer exhibit a remarkable
13 tendency of adhesion and undergo strain hardening, which promotes the formation of the tribolayer over
14 the entire surface and the enhancement of the wear resistance ability. The evolution of wear rate at different
15 linear energy density given in Fig. 11 also suggests such transition of wear resistance performance.
16 Meanwhile, as shown in Fig. 14, the EDS mapping was made to identify the reinforcement WC particles on
17 the worn surface. It is indicated that partial WC particles were partially dissolved in the matrix of MS300, and
18 W element is randomly distributed in the MS300 matrix, which promotes the improvement of mechanical
19 properties.

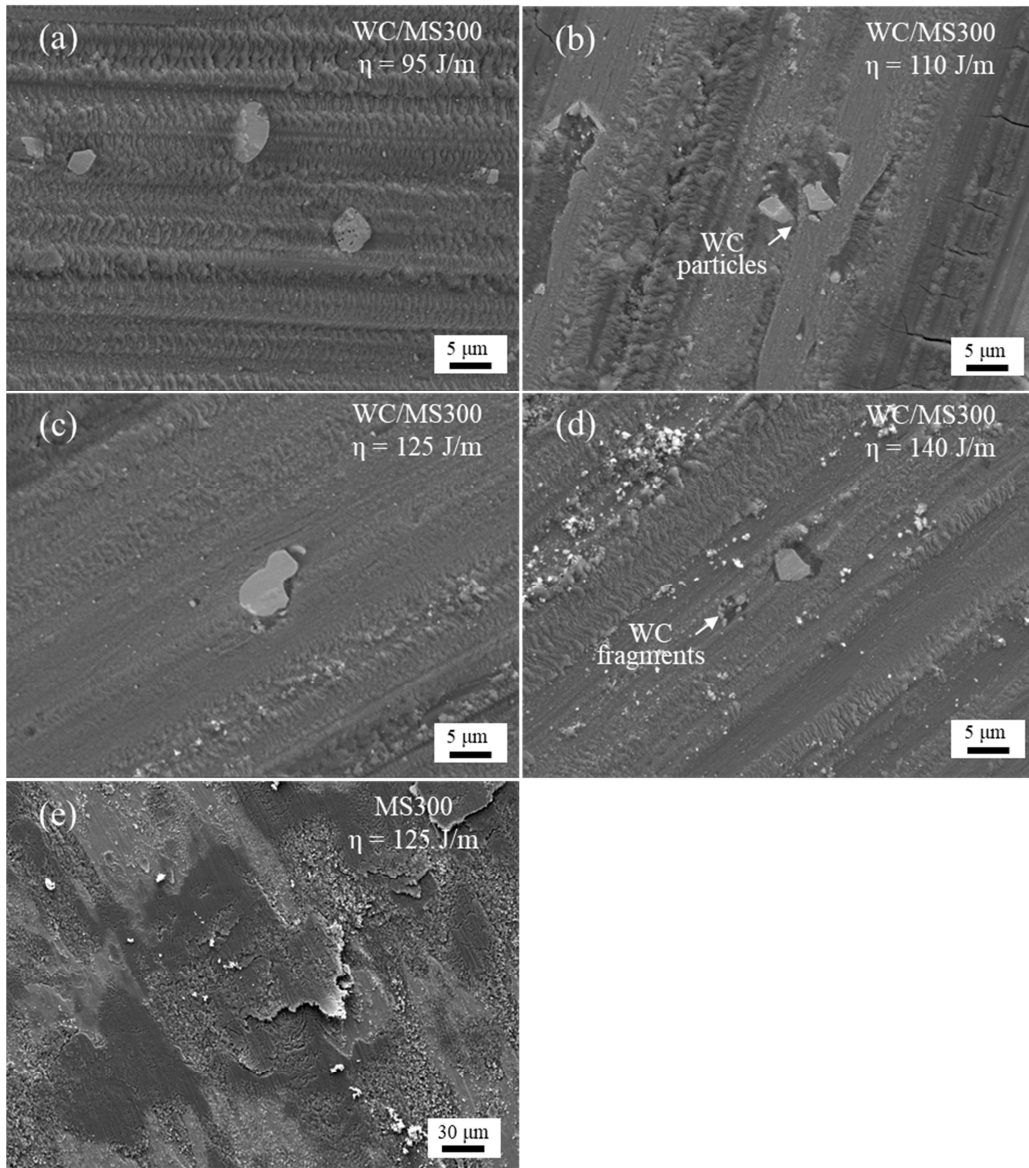
20 As for the WC/MS300 composite fabricated at the highest η value of 140 J/m, the worn surface
21 consists of a number of fragments on the tribolayer, with the fracture of the WC particles and the collapses
22 of the interfacial layer. The similar spalling and cracking on the tribolayer surface were in consistency with
23 the close wear rate value for the composites at 125 and 140 J/m given in Fig. 11. As shown in Fig. 13(d), at
24 the highest energy input, the higher porosity and coarsened microstructure lead to the cracking and peeling
25 of the tribolayer on the worn surface. As a determining factor for wear resistance [37], microhardness has
26 a great influence on the wear performance of the WC/MS300 composite (see Fig. 9 and Fig. 11).

1 As for the pure MS300 sample produced at 125 J/m, much wider and larger wear trace can be found in
2 Fig. 12(e) through the comparison with WC/MS300 composite at the same linear energy density.
3 Meanwhile, the worn morphology of pure MS300 sample is noticed to be consisting of a number of
4 fragments and spalling of the interfacial layer can be found which agrees with the evident higher wear rate
5 value and COF value. With the absence of reinforcement WC particles, severe deformation and material
6 peel-off during the sliding test, which indicates that abrasion was the major wear mechanism [38].



1
2
3
4

Fig. 12 Worn surface morphologies of the samples prepared at different linear energy densities: (a) WC/MS300, 95 J/m, (b) WC/MS300, 110 J/m, (c) WC/MS300, 125 J/m, (d) WC/MS300, 140 J/m, (e) MS300, 125 J/m,

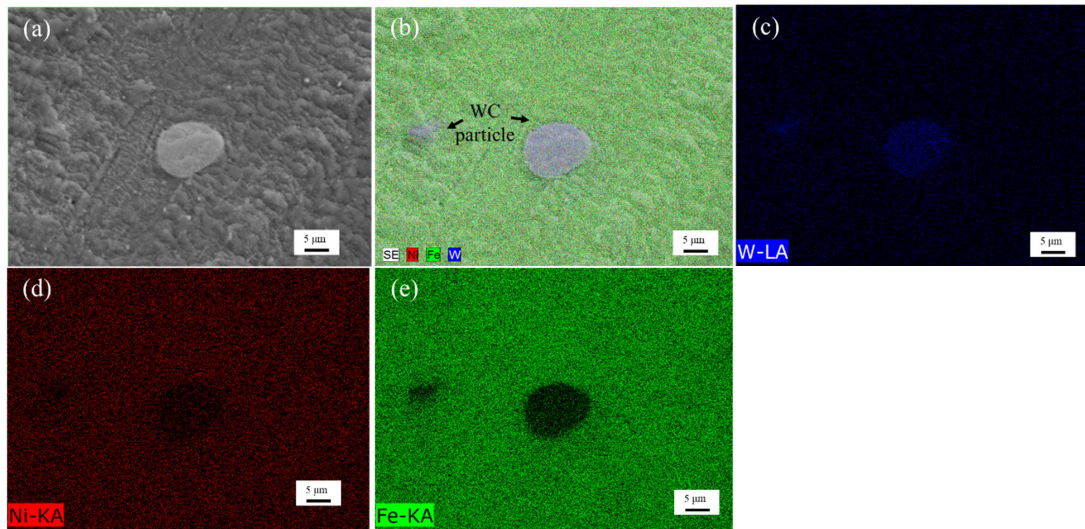


1

2 Fig. 13 Worn tracks at high magnification of the samples prepared at different linear energy densities: (a)

3 WC/MS300, 95 J/m, (b) WC/MS300, 110 J/m, (c) WC/MS300, 125 J/m, (d) WC/MS300, 140 J/m, (e)

4 MS300, 125 J/m.



1

2

Fig. 14 EDS analysis result of the single WC particle remained on the worn surface of the WC/MS300

3

fabricated at 125 J/m.

4. Conclusion

5

In this work, the maraging steel 300 composites reinforced by the WC particles were fabricated by SLM under different laser powers. The present work seeks to provide an effectively method to improve the tribological performance MS300 through the reinforcement of WC particle by selective laser melting.

8

1) The microstructure observation shows that gradient interface as well as diffusion interlayer surrounding the WC particles in MS300 matrix. However, with the increasing linear energy density, the WC particles experienced more sufficient dissolution and such gradient interface was disappeared.

9

10

11

2) After slight increase from 95 J/m, the microhardness rapidly drops as the linear energy density further increases above 110 J/m owing to the linear energy density induced transition of the phase, grain size and defects in the matrix.

12

13

14

3) Friction test shows that an improved wear-resistance at higher linear energy density, whereas the lowest wear rate value and best wear resistance performance was obtained at the linear energy density of 125 J/m. The wear mechanism during was changed from abrasion to adhesion as the linear energy density increases.

15

16

17

1 4) By comparing the WC/MS300 composite with the pure MS300 at the same linear energy density of
2 125 J/m, it can be found that the role reinforced WC particles can evidently increase the microhardness
3 as well as the wear performance.

4 **Acknowledgements**

5 The author Xingchen YAN is grateful to the financial supports by China Scholarship Council (CSC-
6 No. 201504490031) and the funds of Sciences Platform Environment and Capacity Building Projects of
7 GDAS (2016GDASPT-0206, 2017GDASCX-0202, 2017GDASCX-0111, 2018GDASCX-0402 and
8 2018GDASCX-0111); Guangzhou Project of Science & Technology (201604016109, 201704030111);
9 Guangdong province Science and Technology Plan Projects (2015B010122004, 2015B090920003
10 2016B070701020, 2016B090916003, 2017A070702016, 2017B030314122 and 2017A070701027);
11 Guangdong Natural Science Foundation (2016A030312015). Guangzhou Science and Technology Program
12 (201510010095).

13 **Reference**

- 14 [1] J.P. Kruth, L. Froyen, J. Van Vaerenbergh, P. Mercelis, M. Rombouts, B. Lauwers, Selective laser
15 melting of iron-based powder, *J Mater Process Technol*, 149 (2004) 616-622.
- 16 [2] A.V. Gusarov, I. Yadroitsev, P. Bertrand, I. Smurov, Heat transfer modelling and stability analysis of
17 selective laser melting, *Appl Surf Sci*, 254 (2007) 975-979.
- 18 [3] J.H. Tan, W.L.E. Wong, K.W. Dalgarno, An overview of powder granulometry on feedstock and part
19 performance in the selective laser melting process, *Additive Manufacturing*, 18 (2017) 228-255.
- 20 [4] X. Yan, S. Yin, C. Chen, C. Huang, R. Bolot, R. Lupoi, M. Kuang, W. Ma, C. Coddet, H. Liao, M. Liu,
21 Effect of heat treatment on the phase transformation and mechanical properties of Ti6Al4V fabricated by
22 selective laser melting, *J Alloy Compd*, 764 (2018) 1056-1071.
- 23 [5] N. Jones, *Science in three dimensions: the print revolution*, 2012.
- 24 [6] M. Yakout, A. Cadamuro, M.A. Elbestawi, S.C. Veldhuis, The selection of process parameters in
25 additive manufacturing for aerospace alloys, *Int J Adv Manuf Tech*, 92 (2017) 2081-2098.

- 1 [7] A.I.H. Committee, Properties and Selection-- Irons, Steels, and High-performance Alloys, ASM
2 International1990.
- 3 [8] K. Kempen, E. Yasa, L. Thijs, J.P. Kruth, J. Van Humbeeck, Microstructure and mechanical properties
4 of Selective Laser Melted 18Ni-300 steel, Phys Procedia, 12, Part A (2011) 255-263.
- 5 [9] A.G. Demir, B. Previtali, Investigation of remelting and preheating in SLM of 18Ni300 maraging steel
6 as corrective and preventive measures for porosity reduction, Int J Adv Manuf Tech, 93 (2017) 2697-2709.
- 7 [10] <ASM-Handbook-volume-4-Heat-Treating-Asm-Handbook-Asm-Handbook-.pdf>.
- 8 [11] <Saleem Hashmi-Comprehensive Materials Finishing-Elsevier (2016).pdf>, DOI.
- 9 [12] T. Hermann Becker, T. Hermann Becker, D. Dimitrov, D. Dimitrov, The achievable mechanical
10 properties of SLM produced Maraging Steel 300 components, RAPID PROTOTYPING J, 22 (2016) 487-
11 494.
- 12 [13] Y. Bai, Y. Yang, D. Wang, M. Zhang, Influence mechanism of parameters process and mechanical
13 properties evolution mechanism of maraging steel 300 by selective laser melting, Mater Sci Eng A, 703
14 (2017) 116-123.
- 15 [14] A. Dalmau, C. Richard, A. Igual – Muñoz, Degradation mechanisms in martensitic stainless steels:
16 Wear, corrosion and tribocorrosion appraisal, Tribol Int, 121 (2018) 167-179.
- 17 [15] D.D. Gu, W. Meiners, K. Wissenbach, R. Poprawe, Laser additive manufacturing of metallic
18 components: materials, processes and mechanisms, Int Mater Rev, 57 (2013) 133-164.
- 19 [16] T. Sercombe, X. Li, Selective laser melting of aluminium and aluminium metal matrix composites,
20 Mater Technol, 31 (2016) 77-85.
- 21 [17] D.Q. Zhang, Q.Z. Cai, J.H. Liu, J. He, R.D. Li, Microstructural evolution and formation of selective
22 laser melting W-Ni-Cu composite powder, Int J Adv Manuf Tech, 67 (2013) 2233-2242.
- 23 [18] T. Rong, D. Gu, Q. Shi, S. Cao, M. Xia, Effects of tailored gradient interface on wear properties of
24 WC/Inconel 718 composites using selective laser melting, Surf Coat Technol, 307, Part A (2016) 418-427.
- 25 [19] D.D. Gu, W. Meiners, Microstructure characteristics and formation mechanisms of in situ WC
26 cemented carbide based hardmetals prepared by Selective Laser Melting, Mater Sci Eng A-struct, 527
27 (2010) 7585-7592.

- 1 [20] X.P. Li, G. Ji, Z. Chen, A. Addad, Y. Wu, H.W. Wang, J. Vleugels, J. Van Humbeeck, J.P. Kruth,
2 Selective laser melting of nano-TiB₂ decorated AlSi10Mg alloy with high fracture strength and ductility,
3 *Acta Mater*, 129 (2017) 183-193.
- 4 [21] H. Attar, S. Ehtemam-Haghighi, D. Kent, I.V. Okulov, H. Wendrock, M. Bonisch, A.S. Volegov, M.
5 Calin, J. Eckert, M.S. Dargusch, Nanoindentation and wear properties of Ti and Ti-TiB composite materials
6 produced by selective laser melting, *Mater Sci Eng A-struct*, 688 (2017) 20-26.
- 7 [22] B. AlMangour, D. Grzesiak, J.-M. Yang, Selective laser melting of TiB₂/316L stainless steel
8 composites: The roles of powder preparation and hot isostatic pressing post-treatment, *Powder Technol*,
9 309 (2017) 37-48.
- 10 [23] J. Jue, D. Gu, K. Chang, D. Dai, Microstructure evolution and mechanical properties of Al-Al₂O₃
11 composites fabricated by selective laser melting, *Powder Technol*, 310 (2017) 80-91.
- 12 [24] Q. Han, R. Setchi, S.L. Evans, Synthesis and characterisation of advanced ball-milled Al-Al₂O₃
13 nanocomposites for selective laser melting, *Powder Technol*, 297 (2016) 183-192.
- 14 [25] D. Gu, G. Meng, C. Li, W. Meiners, R. Poprawe, Selective laser melting of TiC/Ti bulk
15 nanocomposites: Influence of nanoscale reinforcement, *Scr Mater*, 67 (2012) 185-188.
- 16 [26] D. Gu, H. Wang, D. Dai, P. Yuan, W. Meiners, R. Poprawe, Rapid fabrication of Al-based bulk-form
17 nanocomposites with novel reinforcement and enhanced performance by selective laser melting, *Scr Mater*,
18 96 (2015) 25-28.
- 19 [27] B. Song, S. Dong, C. Coddet, Rapid in situ fabrication of Fe/SiC bulk nanocomposites by selective
20 laser melting directly from a mixed powder of micro-sized Fe and SiC, *Scr Mater*, 75 (2014) 90-93.
- 21 [28] M.X. Guo, J. Zhu, L. Yi, F. Wang, G.J. Li, R.S. Lei, Effects of precipitation and strain-induced
22 martensitic transformation of Fe-C phases on the mechanical properties of Cu-Fe-C alloy, *Mater Sci Eng A*,
23 697 (2017) 119-125.
- 24 [29] D. Gu, J. Ma, H. Chen, K. Lin, L. Xi, Laser additive manufactured WC reinforced Fe-based
25 composites with gradient reinforcement/matrix interface and enhanced performance, *Composite Structures*,
26 192 (2018) 387-396.
- 27 [30] G. Cacciamani, A. Dinsdale, M. Palumbo, A. Pasturel, The Fe-Ni system: Thermodynamic modelling
28 assisted by atomistic calculations, *Intermetallics*, 18 (2010) 1148-1162.

- 1 [31] C.L. Qiu, C. Panwisawas, M. Ward, H.C. Basoalto, J.W. Brooks, M.M. Attallah, On the role of melt
2 flow into the surface structure and porosity development during selective laser melting, *Acta Mater*, 96
3 (2015) 72-79.
- 4 [32] Q. Chen, G. Guillemot, C.-A. Gandin, M. Bellet, Numerical modelling of the impact of energy
5 distribution and Marangoni surface tension on track shape in selective laser melting of ceramic material,
6 *Additive Manufacturing*, 21 (2018) 713-723.
- 7 [33] T. Iida, R.I. Guthrie, *The physical properties of liquid metals*, Clarendon Press, Walton Street, Oxford
8 OX 2 6 DP, UK, 1988.1988.
- 9 [34] X. Yan, C. Huang, C. Chen, R. Bolot, L. Dembinski, R. Huang, W. Ma, H. Liao, M. Liu, Additive
10 manufacturing of WC reinforced maraging steel 300 composites by cold spraying and selective laser
11 melting, *Surf Coat Technol*, DOI <https://doi.org/10.1016/j.surfcoat.2018.03.072>(2018).
- 12 [35] B. Obadele, P. Olubambi, O. Johnson, Effects of TiC addition on properties of laser particle deposited
13 WC–Co–Cr and WC–Ni coatings, *T Nonferr Metal Soc*, 23 (2013) 3634-3642.
- 14 [36] D. Mari, S. Bolognini, G. Feusier, T. Cutard, T. Viatte, W. Benoit, TiMoCN based cermets Part II.
15 Microstructure and room temperature mechanical properties, *International Journal of Refractory Metals and*
16 *Hard Materials*, 21 (2003) 47-53.
- 17 [37] P.K. Deshpande, R.Y. Lin, Wear resistance of WC particle reinforced copper matrix composites and
18 the effect of porosity, *Mater Sci Eng A*, 418 (2006) 137-145.
- 19 [38] S. Yin, C. Chen, X. Yan, X. Feng, R. Jenkins, P. O'Reilly, M. Liu, H. Li, R. Lupoi, The influence of
20 aging temperature and aging time on the mechanical and tribological properties of selective laser melted
21 maraging 18Ni-300 steel, *Additive Manufacturing*, 22 (2018) 592-600.
- 22